nuclear fusion
IAEA

PAPER • OPEN ACCESS

Gas exhaust in the Wendelstein 7-X stellarator during the first divertor operation

To cite this article: U. Wenzel *et al* 2022 *Nucl. Fusion* **62** 096016

View the article online for updates and enhancements.

You may also like

- Radial electric field and density fluctuations measured by Doppler reflectometry during the post-pellet enhanced confinement phase in W7-X
T. Estrada, D. Carralero, T. Windisch et al.

- Measurements and correction of the 1/1 error field in Wendelstein 7-X
S.A. Bozhenkov, M. Otte, C. Biedermann et al.

- Overview of the results from divertor experiments with attached and detached plasmas at Wendelstein 7-X and their implications for steady-state operation
M. Jakubowski, M. Endler, Y. Feng et al.

This content was downloaded from IP address 141.52.248.2 on 17/08/2022 at 14:54

OPEN ACCESS
IOP Publishing | International Atomic Energy Agency Nuclear Fusion
Nucl. Fusion **62** (2022) 096016 (11pp) https://doi.org/10.1088/1741-4326/ac7ac4

Gas exhaust in the Wendelstein 7-X stellarator during the first divertor operation

U. Wenzel*, G. Schlisio, P. Drewelow, M. Krychowiak, R. König, T.S. Pedersen, S. Bozhenkov, V. Haak, A.K. Kharwandikar, S. Lazerson, D. Naujoks, V. Perseo, V. Winters and the W7-X Team[a]

Max-Planck-Institut für Plasmaphysik, Wendelsteinstraße 1, 17491 Greifswald, Germany

E-mail: uwe.wenzel@ipp.mpg.de

Received 1 February 2022, revised 16 June 2022
Accepted for publication 21 June 2022
Published 5 August 2022

Abstract

The optimized superconducting stellarator Wendelstein 7-X (W7-X) is equipped with an island divertor for energy control and efficient pumping. We investigated the performance of the island divertor in terms of gas exhaust. For this purpose we have installed 18 pressure gauges in the vacuum vessel. This allowed us to determine the exhaust efficiency, the leakage, the collection efficiency and the compression ratio of the island divertor. These quantities depended strongly on the magnetic configuration. The best performance was obtained in the high-iota configuration. The exhaust efficiency was 2.9%, significantly higher than in the standard configuration (0.44%), and the maximum neutral compression was about 80. The high-iota configuration appears particularly promising for long-pulse operation of W7-X.

Keywords: stellarator, particle exhaust, neutral pressure

(Some figures may appear in colour only in the online journal)

1. Introduction

Wendelstein 7-X (W7-X) is a modular optimized stellarator experiment equipped with a segmented island divertor [1]. The purely external magnetic field of the stellarator with superconducting coils allows long-pulse operation only limited by mechanical considerations, e.g. heating and cooling capabilities, and heat exhaust. In its first divertor operation, an inertially cooled graphite divertor was used to gain insights into divertor operation [2]. The inertially cooled divertor limited the input energy, but allowed for routine plasma pulses with a duration of up to 100 s.

An important aspect of divertor operation is particle exhaust, a fundamental part of the fusion fuel cycle. Plasma particles neutralize at the wall, being either absorbed or released as neutral gas. Large fractions of neutralized particles are recycled into the plasma [3], and a smaller part reaches the sub-divertor volume though the pumping gap. The recycling flux acts as the dominant the particle source in the plasma and sustains the plasma density along with the external fueling, i.e. gas puff, hydrogen ice pellet injection and neutral beam injection. Successful divertor operation is achieved if a large fraction of these neutral particles are guided to a permanent sink, e.g. a vacuum pump, for further treatment, such as fuel recovery and ash removal.

Another fueling source is the wall source. While the above mentioned external sources can be feedback controlled, the wall source cannot. Particles can be deposited in the walls and released when the walls heat up by plasma wall interaction. A detailed study of long-pulse discharges in W7-X showed that the density control was lost at the moment when the wall source exceeded the amount of pumped particles [4]. Therefore, a sufficiently large particle exhaust is necessary to ensure density control and to close the fuel cycle in a future reactor.

In the article, we study the particle exhaust in W7-X and characterize the performance of the island divertor in this respect. We confine ourselves to the operation phase OP1.2b

* Author to whom any correspondence should be addressed.
[a] See Klinger *et al* 2019 (https://doi.org/10.1088/1741-4326/ab03a7) for the W7-X Team.

Original content from this work may be used under the terms of the Creative Commons Attribution 4.0 licence. Any further distribution of this work must maintain attribution to the author(s) and the title of the work, journal citation and DOI.

 © EURATOM 2022

in which the inertially cooled graphite divertor was used. A detailed description of the island divertor and its physical properties in this operation phase is given in [14]. The plasma in the island divertor can be in the detached or attached state. If the divertor plasma radiates close to the divertor targets, the state is called attached. At high plasma radiation, a transition to the detached state is observed, in which the energy deposition on the target plates is greatly reduced and the radiation zone moves away from the target plates [14, 15].

In our study we consider attached divertor plasmas in two different magnetic configurations with very different exhaust performances. In section 2, we begin with a description of the island divertor geometry and the pumping capability in operation phase OP1.2b. In section 3, we continue with the basic quantities that characterize a divertor in terms of particle exhaust. The diagnostic systems we used are described in section 4. The experimental results are presented in section 5 for both the magnetic standard and the high-iota configuration. It will be shown that in the high-iota configuration, higher sub-divertor pressure can be achieved and more particles can be pumped out. The reasons for this surprising result are discussed in section 6. Also in this section, we extrapolate the results to the next operation phase OP2 of W7-X. For OP2, the inertially cooled divertor was replaced by an actively cooled divertor. We close the article with section 7 in which we summarize the experimentally determined physical quantities of the island divertor which are important for the particle exhaust. Uncertainty considerations are summarized in the appendix.

There is another important aspect of particle exhaust, namely the removal of helium. In a reactor the helium ash needs to be pumped efficiently in order not to dilute the burning plasma. This issue is not addressed in the present article and must be reserved for future studies.

2. Divertor geometry and pumping

The W7-X divertor is a segmented island divertor of the open type [5] and makes use of the naturally occurring magnetic islands at rational values of the rotational transform ι, which are intersected by target plates. An upper and a lower divertor are located in each of the five symmetric stellarator modules. In the *standard* configuration with $\iota = 5/5$, periodicity results in five separate island tubes outside the last closed flux surface winding around the core plasma helically, while in the *high-iota* configuration with $\iota = 5/4$, a single island tube in the edge region generates four islands. The magnetic geometry, and consequently the particle deposition on the divertor targets, is very different between these configurations.

Each divertor is divided in itself in two main parts, the *high-iota* and *low-iota* target plates utilized for different magnetic configurations [6]. While the *high-iota* part is only used in the *high-iota* magnetic configuration, the *low-iota* part is used for all other magnetic configurations.

In the operation phase OP1.2 an inertially-cooled graphite divertor was used with a sub-divertor space divided between the two separately pumped parts. The sub-divertor volumes of one divertor unit were estimated from CAD with 0.512 m^3 for the low-iota part and 0.047 m^3 for the high-iota part. Both volumes are actively pumped with turbo-molecular pumps connected via the pumping duct (AEH and AEP port respectively) [7]. Figure 1 illustrates the target geometry and both the pumping lines of the high- and low-iota parts of divertor. The low-iota part can be easily identified because it consists of vertical and horizontal target plates while the high-iota part consists only of a horizontal target. The effective pumping speed S_{eff} at the *low-iota* pumping duct (end of the pump line in the sub-divertor volume) was experimentally determined to be $2350 \pm 118\ \mathrm{l\,s^{-1}}$ and at the *high-iota* pumping duct to be $1180 \pm 59\ \mathrm{l\,s^{-1}}$.

While efforts have been made to reduce gas leakage from the sub-divertor space towards the plasma chamber by adding closure plates, perfect tightness could not be achieved and a fraction of gas is not pumped but lost back to the main chamber.

The neutrals enter the sub-divertor volume through the pumping gap. Figure 2 shows cross sections of the high-iota part and of the low-iota part of the divertor, illustrating the different pumping gap geometries.

The size of the pumping gap was optimized in [8]. There is an optimum size for which the sub-divertor pressure is maximum. In the low-iota region, there is an additional cover of the sub-divertor volume which is not installed in the high-iota region and was not considered in the optimization procedure. This is to protect the sub-divertor volume from plasma radiation.

3. Definition of the experimentally determined quantities

Exhausting the gas in the divertor is a multi-step process. Plasma particles are neutralized at the target plates, transported to the pumping gap and through the sub-divertor volume to the pumping duct, where they are captured by the pumps and removed from the system. Particles enter the sub-divertor through the pumping gap at a pressure p_{gap}, propagate through the volume and arrive at the pumping duct, yielding a (typically lower) pressure p_{duct}. The latter is determined by the gas tightness of the sub-divertor volume, the position and dimension of the pumping gap, the conductance in the sub-divertor volume and finally by the design of the pumping system, i.e. the effective pumping speed at the pumping duct S_{eff}.

Due to the linear dependence of the exhaust rate $\Gamma_{\mathrm{ex}} = p_{\mathrm{duct}} \cdot S_{\mathrm{eff}}$ on the pressure p_{duct} and the effective pumping speed of the turbo pumps S_{eff}, the divertor pressure provides greater leverage on the particle exhaust rate compared to the expensive and technically limited pumping speed increase.

The *particle collection efficiency* (PCE) is defined as the ratio of the target flux Γ_{t} and the flux through the pumping gap into the sub-divertor volume Γ_{gap}. It describes the share of particles entering the divertor system and is determined by the plasma parameters and the interaction with the divertor target plates.

$$\mathrm{PCE} = \Gamma_{\mathrm{gap}}/\Gamma_{\mathrm{t}}. \tag{1}$$

Not every neutral particle in the sub-divertor volume will be exhausted (Γ_{ex}). Some will leak out of the divertor (Γ_{leak}),

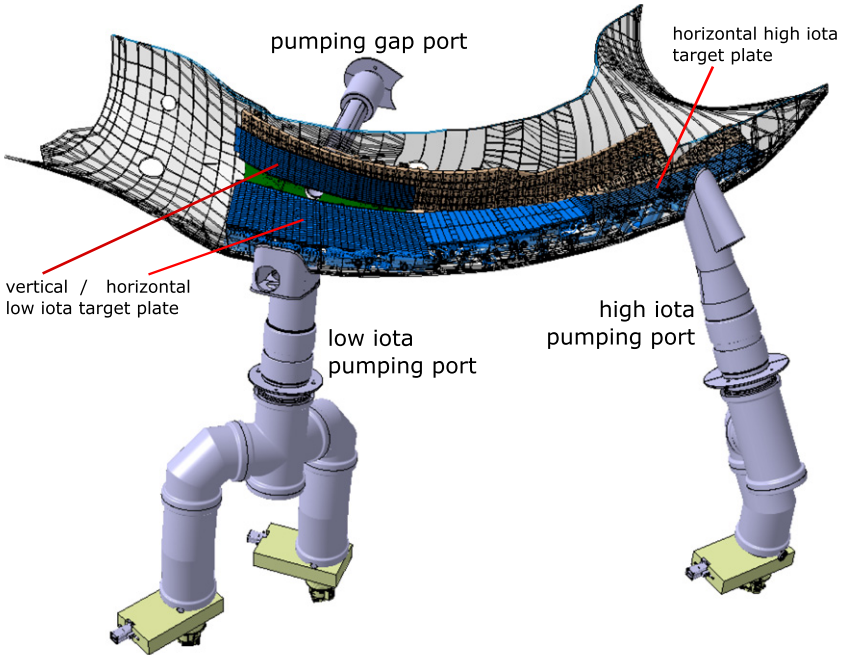

Figure 1. Geometry of the island divertor targets and the pumping lines of the low-iota sub-divertor region (AEH, left) and the high-iota sub-divertor region (AEP, right). The divertor is shown in blue, pumping gap panels in green. On top, a port can be seen (AEI) accessing the pumping gap for pressure measurement (see figure 3). The lower part of the plasma vessel is shown as a semitransparent manifold with mesh surface and port openings.

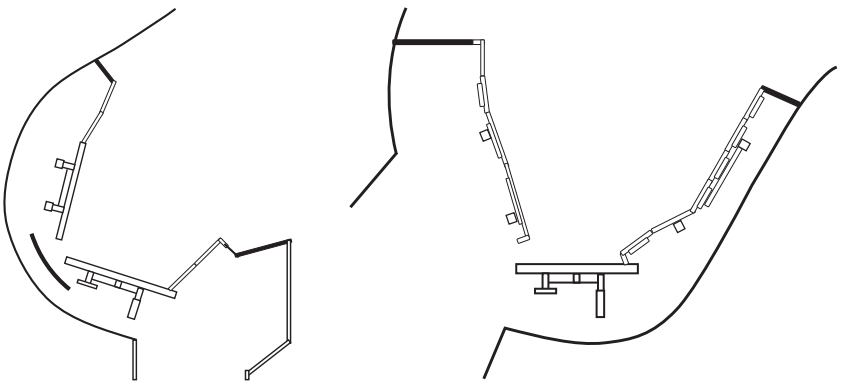

Figure 2. Cross sections of the divertor at the pumping ports: left: low-iota part of the divertor with both the vertical and horizontal targets and the baffle structures. The vessel opening to the bottom is the pumping port AEH. Right: high-iota part of the divertor with the horizontal target and the baffle structures. The vessel opening to the left is the pumping port AEP.

i.e. it holds

$$\Gamma_{\mathrm{gap}} = \Gamma_{\mathrm{ex}} + \Gamma_{\mathrm{leak}}. \tag{2}$$

This allows us to define the *particle removal efficiency* (PRE) as

$$\mathrm{PRE} = \Gamma_{\mathrm{ex}}/\Gamma_{\mathrm{gap}}. \tag{3}$$

With the defined quantities PRE and PCE, we obtain the exhaust efficiency ε as the ratio of the exhaust flux to the neutral flux from the divertor targets

$$\varepsilon = \Gamma_{\mathrm{ex}}/\Gamma_{\mathrm{t}} = \mathrm{PCE} * \mathrm{PRE}. \tag{4}$$

These quantities can be used to characterize the exhaust performance for the working gas hydrogen (or deuterium) as well as for the impurity helium. In the case of hydrogen, the fluxes have the unit molecules s^{-1} while in the case of helium the unit is atoms s^{-1}.

Another typical figure-of-merit is the *compression* given by the ratio of the sub-divertor pressure and the main chamber pressure, typically measured in a midplane position. The compression ratio indicates how well the particles can be exhausted from the nuclear fusion device. It is frequently used for comparison among different divertor concepts. The selection of the sub-divertor pressure measurement position is often determined by the available gauge positions. In the following, the pressure measurement at the pumping duct is used as reference for the sub-divertor pressure, as it is the relevant pressure to determine particle exhaust through the pump duct.

In order to determine the compression and the efficiency quantities of the island divertor of W7-X, we have to measure target fluxes and the sub-divertor pressures. The diagnostic systems necessary for measuring pressures and fluxes are introduced in the next section.

Table 1. Overview of the in-vessel pressure gauges used in OP1.2b, with their poloidal and toroidal positions.

Name	Module	Position	Gauge type	Field strength (T)
AEE11	1	Midplane	APG	1.65
AEA21	2	Midplane	CCPG	1.98
AEE30	3	Midplane	APG	1.62
AEE41	4	Midplane	CCPG	1.91
AEE50	5	Midplane	APG	1.60
AEH11	1	Upper low-iota pumping port	APG	1.78
AEH21	2	Upper low-iota pumping port	APG	1.78
AEH31	3	Upper low-iota pumping port	APG	1.77
AEH41	4	Upper low-iota pumping port	CCPG	1.79
AEH51	5	Upper low-iota pumping port	APG	1.85
AEH30	3	Lower low-iota pumping port	CCPG	1.85
AEH50	5	Lower low-iota pumping port	APG	1.64
AEP30	3	Upper high-iota pumping port	CCPG	1.57
AEP50	5	Upper high-iota pumping port	APG	1.60
AEP51	5	Lower high-iota pumping port	CCPG	1.60
AEI30	3	Lower pumping gap	CCPG	2.18
AEI50	5	Lower pumping gap	CCPG	2.19
AEI51	5	Upper pumping gap	CCPG	2.17

4. Diagnostics

4.1. Neutral pressure measurement

A set of 18 in-vessel pressure gauges was installed in W7-X in several toroidally and poloidally distributed positions with local magnetic field strengths between 1.6 T and 2.2 T. Due to the demanding environment of strong magnetic fields and low pressures, hot-cathode ionization gauges specially designed for fusion applications were used. Depending on the cathode type they are either called *ASDEX pressure gauges* (APGs) or *crystal cathode pressure gauges* (CCPGs). APGs are equipped with tungsten cathodes [12] while CCPGs have crystal cathodes, improving the robustness of the gauge in long pulse operation. The CCPGs used in W7-X were equipped with cathodes made from single crystalline LaB_6 rods [17]. While APGs suffered from severe cathode problems [19], no such problems were observed with the CCPGs during the operation phase OP1.2b [18].

Table 1 gives a survey of the different positions of the gauges. Five gauges were located in the midplane with one in each stellarator module. They were mounted at the end of the ports (about 10 cm from the plasma vessel contour). In these positions they were exposed to the direct flux of neutrals.

The remaining gauges were distributed in the sub-divertor space in both the high- and low-iota parts of the divertor. The former was equipped with gauges in the pumping port only (AEP port), while the latter had gauges in the pumping port (AEH port) as well in close proximity to the pumping gap (AEI port). An illustration of the pressure gauges in the low-iota part of the island divertor is given in figure 3.

The toroidal coverage allows investigation of symmetry aspects, while the poloidal distribution of gauges gives insight into the neutral compression and exhaust behavior of the W7-X island divertor.

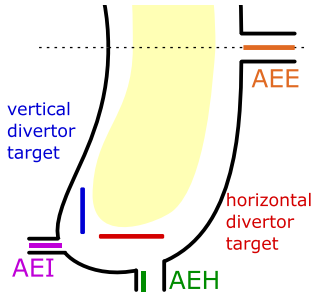

Figure 3. Schematic illustration of the positions of the in-vessel pressure gauges in the low-iota part of the island divertor and in the midplane. Neutral compression is defined as the pressure ratio in the pumping duct (green) to midplane. Adapted from [18], with the permission of AIP Publishing.

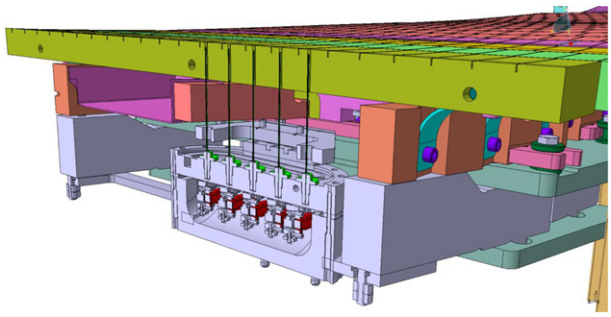

Figure 4. Gas injection system with the injector box with five fast piezo valves and the capillary nozzles.

4.2. Hydrogen flux measurement

In order to derive the particle fluxes from the divertor targets, visible light cameras with H_α filters were used. W7-X was equipped with a set of 10 cameras, one for each divertor target

Table 2. Plasma parameters of the two experiments used for the characterization of particle exhaust.

	Standard configuration	High-iota configuration
Experiment number	20 180 905.30	20 180 808.12
Line-integrated electron density	11×10^{19} m^{-2}	11×10^{19} m^{-2}
ECRH power	6 MW	5 MW
Stored energy W_{dia}	700 kJ	600 kJ
Fraction of radiated power f	0.47	0.41
Divertor condition[a]	Attached	Attached

[a]Here the definition of attached plasmas is used, that the fraction of the radiated power f is not more than 0.75.

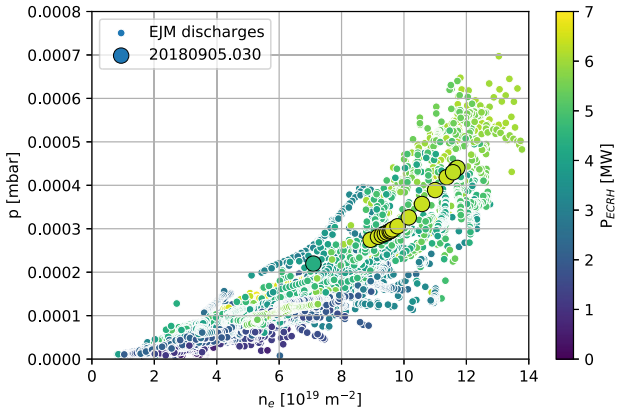

Figure 5. Averaged neutral pressure in the low-iota pumping ports over line-integrated density n_e for the magnetic standard configuration and heating power P_{ECRH} color coded. Plasma experiments were split into 200 ms parts each plotted separately.

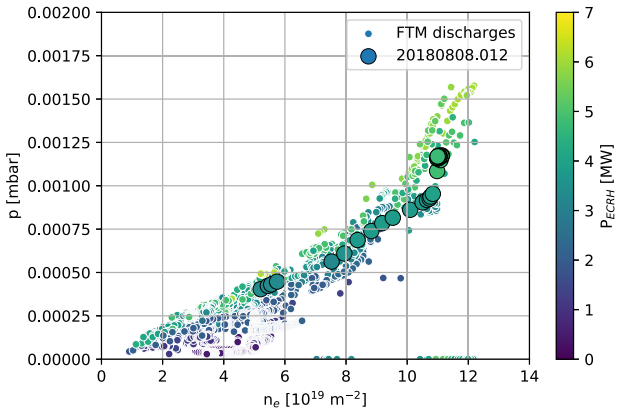

Figure 6. Averaged neutral pressure in the high-iota pumping ports over line-integrated density n_e for the magnetic high-iota configuration and heating power P_{ECRH} color coded. Plasma experiments were split into 200 ms parts each plotted separately.

[3]. The cameras could be operated with different interference filters to measure both hydrogen lines and carbon lines. From the measured line integrated intensity I the neutral flux Γ can be derived using the relation $\Gamma = 4^*\pi^*S/(XB)^*I$ where S/XB is the atomic physics factor (S is the ionization rate, X is the excitation rate, and B is the so-called branching ratio). The flux relation can be applied in this form for atomic and ionic lines, e.g. in order to derive the impurity influx from the carbon ion spectral lines [10].

For the H_α radiation, the situation is more complicated because mainly molecules leave the target and H_α radiation is produced both during the dissociation of molecules and during the excitation of hydrogen atoms. Following [11], the flux relation can also be used in this case by replacing the factor S/XB by an effective value $(S/XB)_{\mathrm{eff}}$. For H_α radiation, the flux relation reads as follows: $\Gamma_{\mathrm{total}} = 4^*\pi^*(S/XB)^*_{\mathrm{eff}}I$ where $\Gamma_{\mathrm{total}} = \Gamma_{\mathrm{H}} + 2\Gamma_{\mathrm{H2}}$ is the total particle flux. The experiments described in [11] showed that the appropriate value for $(S/XB)_{\mathrm{eff}}$ is about 30 for wall components that were not actively heated, which is nearly twice the original S/XB value [13].

There are always particle losses at the edge of the deposition area that do not contribute to the hydrogen emission. This systematic error leads to the calculated particle flux representing the lower limit. The greater the electron density in the ionisation region, the smaller the systematic error.

The pumped particle flux consists only of hydrogen molecules. In order to compare the total particle flux from the divertor targets with the pumped particle flux, we have to use the equivalent molecular flux which is given by $\Gamma_{\mathrm{mol}} = \Gamma_{\mathrm{total}}/2$.

4.3. Divertor gas injection

The divertor gas injection system was also used for the characterization of the particle exhaust. It is part of the helium beam diagnostic [9]. In the experimental campaign OP1.2, two identical divertor gas injection systems were operated: one in the lower divertor module (machine half module 30) and one in the upper divertor module (machine half module 51). Each system features a box with five fast piezo valves (marked in red in figure 4) attached to the back side of the divertor.

The system was designed to provide a number of gas types for many purposes: helium and neon for emission spectroscopy, argon for impurity transport studies, neon and nitrogen for edge radiative cooling experiments, and hydrogen for fueling with e.g. density feedback. The gas leaves the box through thin capillary nozzles of about 10 cm length and is injected directly into the plasma at the front side of the divertor. The nozzles were brazed into stainless steel adapters (marked in green in figure 4) screwed into the base plate of the valve box without dedicated sealing. This caused a fraction of the gas flow to leak at the back side of the divertor, thereby increasing the neutral gas pressure in the low-iota sub-divertor region.

In order to determine the leak rate of the sub-divertor region, we used the injection of hydrogen with a pre-programmed sharp pulse with a minimum length of 10 ms. The parasitic gas puff was directly detected by the pressure gauges in positions AEH51 and AEI51 (see table 1). After the end of

the gas pulse, the pressure in the sub-divertor volume dropped exponentially

$$p(t) = p_{\max} * \exp\left(-\frac{t}{\tau}\right).$$

From the decay time constant τ, the leak rate of the low-iota sub-divertor region was determined.

5. Results

We have studied the particle exhaust in two magnetic configurations: standard and high-iota configuration. For the comparison, we will use two plasma experiments with similar plasma parameters (see table 2 for details).

Figures 5 and 6 show scatter plots with experiments that were heated with electron cyclotron waves (electron cyclotron resonance heating—ECRH) only. The two selected plasma experiments are depicted by the larger symbols. Several time points per experiment were considered for this plot. Their time interval was 200 ms. The scatter plots show the general trend that the pressures in the pumping ducts were significantly higher in the high-iota configuration. The neutral pressures increased with the electron density and with the heating power. Both selected experiments had maximum electron-density at high heating power. However, there was a much larger variation of the neutral pressure at maximum electron density in the magnetic standard configuration. It is $\pm 50\%$. This might be due to the larger number of experiments with different heating powers which were carried out in this magnetic configuration.

The particle deposition on the targets is very different, but this is to be expected because of the differences in the magnetic configurations. Figure 7 shows the H_α images of both configurations. The different parts of the divertor, i.e. the targets and baffles, are schematically drawn as follows: horizontal target (high-iota, low-iota and the middle part), vertical target and baffles. In the standard configuration the particles impinge on the vertical and horizontal targets of the low-iota tail. In the high-iota configuration they hit mainly the horizontal target at the high-iota tail. There is also some smaller particle deposition on the vertical target. Note that the sub-divertor spaces below the low-iota and high-iota strike lines are separated. Thus, in the high-iota configuration a significant pressure is only expected in the high-iota sub-divertor region while in the magnetic standard configuration, a significant pressure is only expected in the low-iota sub-divertor region.

5.1. Standard configuration

Figure 8 shows the time traces of the plasma experiment in the magnetic standard configuration. A maximum pressure in the low-iota pumping duct of 4×10^{-4} mbar was measured giving an exhaust rate of 4×10^{-4} mbar $\times$ 2350 l s^{-1} = 0.94 $\pm$ 0.19 mbar l s^{-1}. We have checked the modular symmetry of the neutral pressures in the upper pumping ducts using the pressure gauges in several pumping ports. No significant asymmetry was found. This allows the extrapolation of the total exhaust flux for all ten divertor modules by a factor of 10, i.e. it is 9.4 $\pm$ 1.9 mbar l s^{-1}.

The pressure near the pumping gap (AEI position) is significantly higher by a factor of 1.5 while the pressure in the high-iota sub-divertor (AEP position) is smaller but not as small as expected by the decoupling of the sub-divertor volumes.

In order to determine the leakage we used the parasitic gas pulse of the gas injection system into the low-iota sub-divertor volume (see figure 9).

We could observe the pump-out of a parasitic hydrogen pulse which is due to the leakage of the low-iota sub-divertor and the pumping. The decay was exponential as expected and the $1/e$ decay time τ was 0.14 s (see figure 9). With this decay time we found an effective removal speed of the gas pulse S_r

$$S_r = V_{li}/\tau = 5121/0.14\,\mathrm{s} = 3657 \pm 371\,\mathrm{s}^{-1},$$

where V_{li} is the sub-divertor volume under the low-iota target. The accuracy of the removal speed was determined by the accuracy of the sub-divertor volume which was measured in the CAD model of the divertor. It was about 10%. The effective removal speed S_r was larger than the effective pumping speed S_{eff} due to the leakage Γ_{leak}.

The particle removal efficiency by the turbo pumps was estimated as follows

$$\mathrm{PRE} = \frac{\Gamma_{ex}}{\Gamma_{gap}} = \frac{\Gamma_{ex}}{\Gamma_{leak} + \Gamma_{ex}} = \frac{p_{duct} * S_{eff}}{p_{average} * S_r},$$

where $p_{average}$ is an average sub-divertor pressure. With the approximation $p_{average} \approx p_{duct}$ we arrive at

$$\mathrm{PRE} \approx 2350/3657 \approx 0.64 \pm 0.1.$$

The approximation is justified because the exhaust flux is larger than the leak flux, but it causes a systematic error which could be as large as -20%.

In order to derive the particle exhaust efficiency, we have estimated the total target flux. First we summarized the measured H_α photon fluxes over the whole target (see figure 10). During the flat-top phase we got 2.2×10^{19} photons s^{-1} sr^{-1} taking into account all parts shown in figure 10. This gave a total particle flux of 8.3×10^{21} particles s^{-1} using the conversion factor $4 \times \pi \times (S/XB)_{eff}$. The equivalent molecular flux was 5.5×10^{21} molecules s^{-1}. The accuracy of the particle fluxes was 10% (see appendix).

In order to compare the target flux with the exhaust flux, we had to convert the exhaust flux 0.94 mbar l s^{-1} using the gas equation with $T = 300$ K. We got 0.022×10^{21} molecules s^{-1} and thus for the exhaust efficiency

$$\varepsilon = \Gamma_{ex}/\Gamma_t = 0.0044 \pm 0.0132. \quad (5)$$

Finally, we obtained for the PCE, the ratio of the flux into the sub-divertor space to the target flux, a value of 0.0069 $\pm$ 0.0028 using the relation $\varepsilon = \mathrm{PCE} \cdot \mathrm{PRE}$.

5.2. High iota configuration

Figure 11 shows the time traces of the plasma experiment in the high-iota configuration. A maximum pressure in the high-iota pumping duct (pumping port AEP) of 1.5×10^{-3} mbar was measured giving an exhaust rate of 1.5×10^{-3}

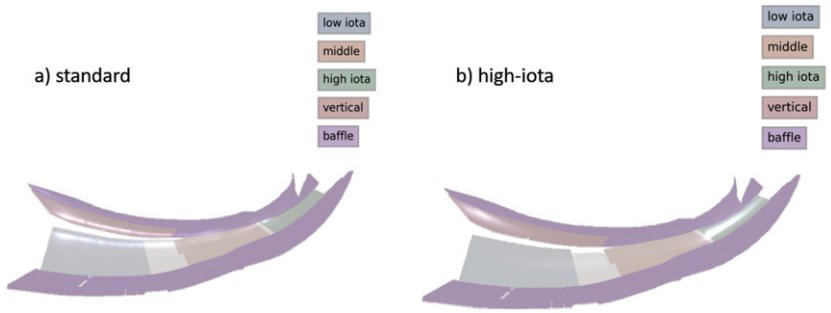

Figure 7. Strike line patterns on the divertor targets in the magnetic standard (*a*) and high-iota configuration (*b*) (see the white contours of the H_α emission). The different parts of the island divertor have been added to the experimentally obtained H_α images.

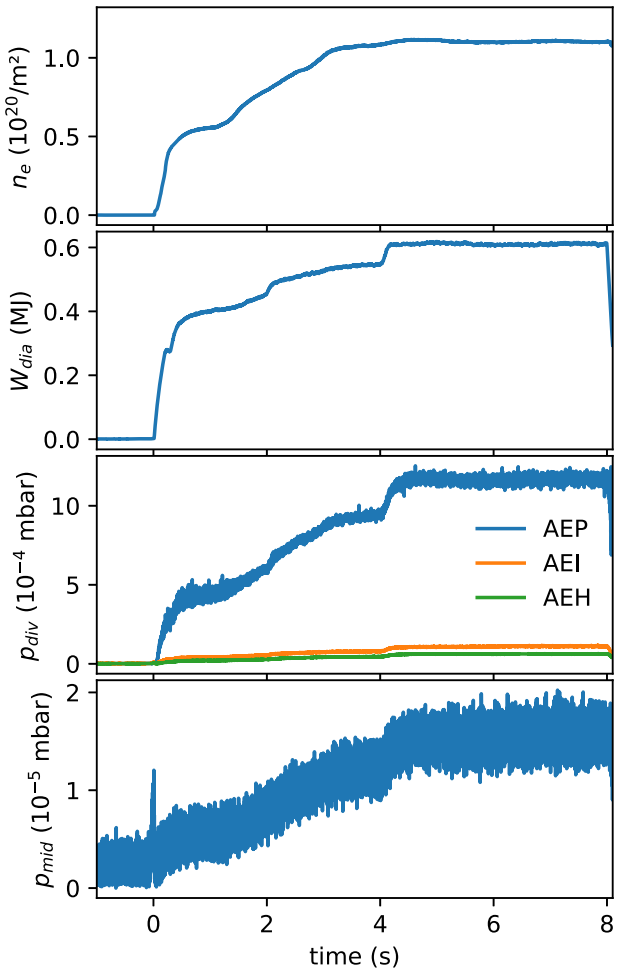

Figure 8. Time traces of the plasma experiment in magnetic standard configuration: line-averaged electron density n_e, confined energy W_{dia}, sub-divertor pressures (pumping ducts of the low-iota and high-iota sub-divertor regions, pumping gap (near the AEI port) and midplane pressure. At 4 s, the neutral pressure in the pumping duct (pumping port AEH) was 0.0004 mbar.

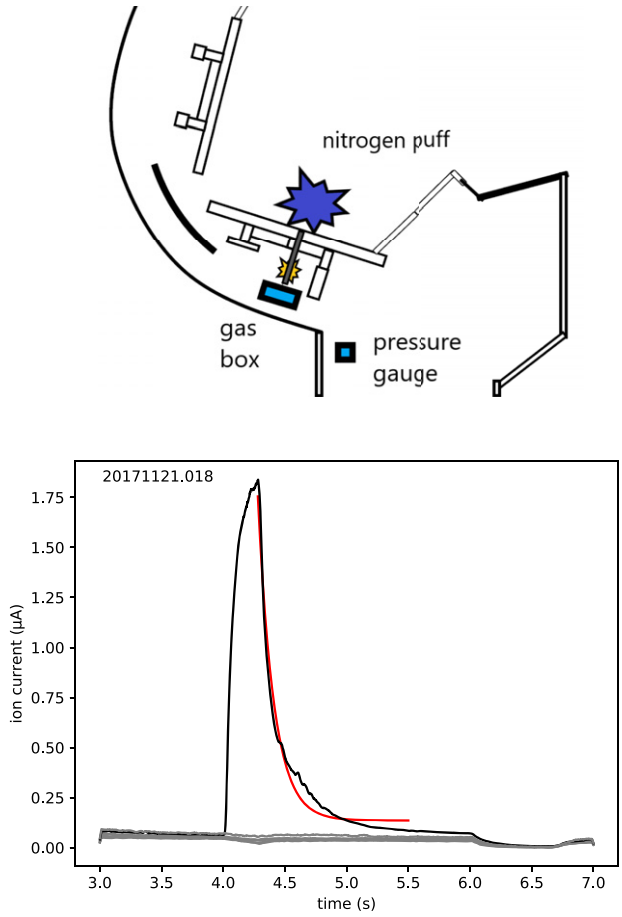

Figure 9. W7-X plasma experiment (2017-11-21.18) with gas injection (nitrogen) into the divertor in half module 51 for the measurement of the pump-out time of the sub-divertor. On top: illustration of the measuring principle with pressure gauge and gas injection box. Nitrogen is injected into the divertor (blue star) but also into the sub-divertor volume (orange star). At bottom: ion currents over time of six pressure gauges in the pumping ducts (AEH11, AEH21, AEH31, AEH41, AEH51, AEH50). Only the pressure gauge AEH51 detected the nitrogen pulse (black line). The data was fitted by an exponential function (red line). The nitrogen pressure decayed exponentially with an 1/*e* decay time of 0.14 s.

mbar $\times$ 1180 l s^{-1} = 1.8 $\pm$ 0.36 mbar l s^{-1}. The total exhaust flux for all ten divertor modules was 18 $\pm$ 3.6 mbar l s^{-1}. The pressures in the low-iota sub-divertor region were very low because of the decoupling from high-iota sub-divertor region.

For the high-iota configuration we did not have the possibility to inject a test pulse into the sub-divertor volume. Therefore we could determine only the exhaust efficiency but not the particle collection and particle removal efficiencies (PCE and PRE). We applied the same procedure as described above to the H_α image. First we summarized the measured H_α photon fluxes over the whole target (see figure 12). During

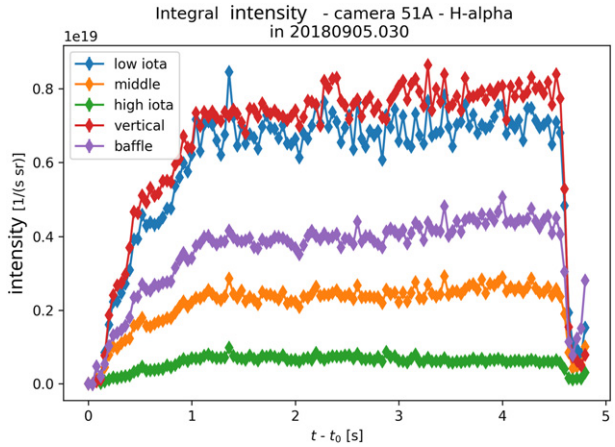

Figure 10. H_α intensities as a function of the experiment (20 180 905.30) time from the different parts of the divertor. Magnetic configuration was the standard configuration.

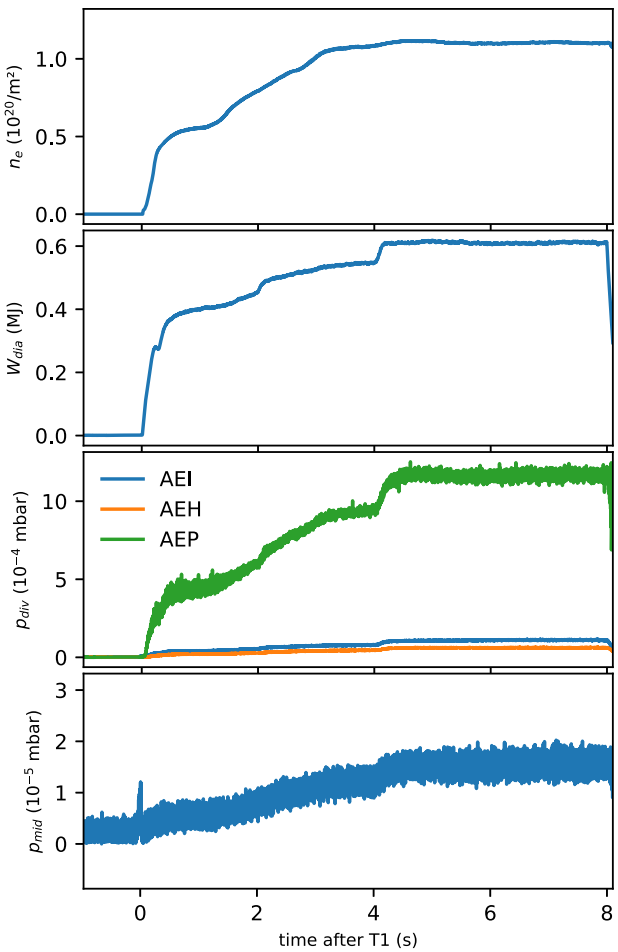

Figure 11. Time traces of the plasma experiment in high-iota configuration: electron density, confined energy, sub-divertor pressures and midplane pressure. At 6s, the neutral pressure in the pumping duct (pumping port AEP) was 0.0015 mbar.

the flat-top phase we got 0.6×10^{19} photons s^{-1} sr^{-1} taking into account all parts shown in figure 12. This gave a total particle flux of 2.2×10^{21} particles s^{-1} using the conversion factor $4 \times \pi \times (S/XB)_{eff}$. The equivalent molecular flux was

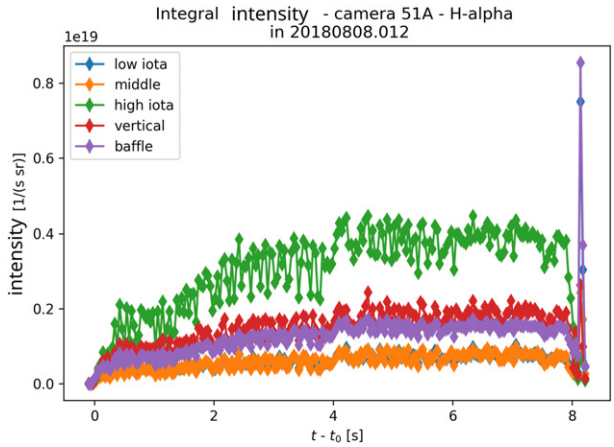

Figure 12. H_α intensities as a function of the experiment (20 180 808.12) time from the different parts of the divertor. Magnetic configuration was the high-iota configuration.

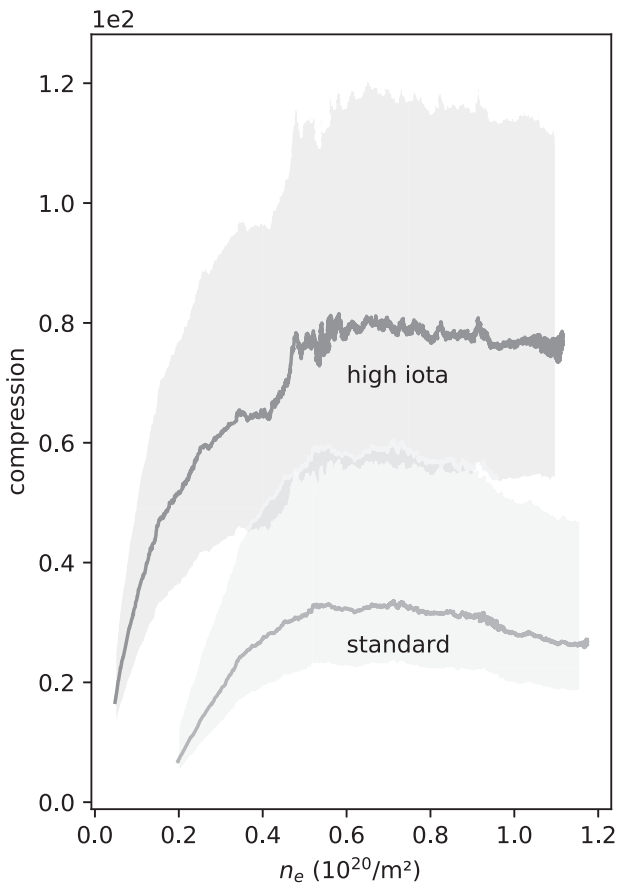

Figure 13. Compression ratios over electron density for both studied magnetic configurations.

1.5×10^{21} molecules s^{-1}. The accuracy of the particle fluxes was 10% (see appendix).

The exhaust flux 1.8 mbar l s^{-1} corresponds to 0.044×10^{21} molecules s^{-1}. The exhaust efficiency in the high-iota configuration was

$$\varepsilon = \Gamma_{ex}/\Gamma_t = 0.029 \pm 0.009. \quad (6)$$

6. Discussion

Both in standard and high-iota configurations the neutrals were compressed by the island divertor. For the sub-divertor pressure, the pressure in the pump ducts were used. Figure 13 shows the compression ratios over the electron density. The compression ratio rises with density up to a value of 5×10^{19} m^{-2}. Above this value the compression is almost an independent constant, i.e. the compression is maximum. In the high-iota configuration, the maximum compression ratio is 80 while in the standard configuration, it is about 30.

We compare the obtained compression ratio in the magnetic standard configuration with the result of the simulation [8]. In the simulation, a compression of 170 was found. However, there was no pumping in the sub-divertor and no leakage. The only back flux from the sub-divertor to the plasma volume was through the pumping gap. Furthermore, such simulations assumed an average plasma beta value of 4% and did not include radiation from plasma impurities. The simulated compression ratio therefore gives an upper limit which is determined by the dimension of the pumping gap and the target geometry. The measured maximum compression ratio is 30 which is significantly lower because of (a) the pumping by the turbo pumps, (b) leakage in addition to the back flow through the pumping gap, and (c) the lower neutral density in front of the pumping duct compared to the calculated average neutral density in the sub-divertor volume. Other simulations were performed more closely to the OP1.2b experimental operational space [20]. An attached divertor plasma was used with a lower density compared to the presented experiments. These simulations showed lower compression values, in the range of 40–60.

It is well known that the distance of the strike line from the pumping gap strongly influences the neutral compression in divertor geometries. This effect has been documented through a systematic study of rotational transform variations in W7-X [16]. When comparing the results presented here one must recognize that the standard configuration discharge presented here was conducted with -500 A of planar coil current correction (20 180 905.30). Such correction was shown to place the strike lines farther from the pumping gap than would be desired in the ideal case (used in modeling). It should also be noted that 2000 A of control coil current were used in this discharge resulting in a radial growth of the 5/5 island chain. This has the effect of changing both the divertor strike points and connection lengths. A systematic experimental study of the control coils effect on divertor strike line and performance has yet to be conducted.

We found a large difference in gas exhaust when we compared both magnetic configurations. In the high-iota configuration the exhaust efficiency was a factor of 6.6 higher than in the standard configuration (0.029 vs 0.0044). The exhaust efficiency is determined by two factors: PCE and PRE. The difference might be caused by one of the factors or by both, i.e. the leakage of the magnetic standard configuration might be higher and/or the collection efficiency is lower in the standard configuration. From the detailed analysis it became clear that the PCE is low in the magnetic standard configuration. It is only 0.0069. Since we do not expect large differences in the leakage from both sub-divertor volumes, we assume that the low PCE is the reason for the low exhaust efficiency. In the high-iota configuration there is one island in the divertor while in the standard configuration, there are two. The geometry with one island is apparently more effective in respect to particle collection. Another reason for the better particle collection could be the lack of radiation shielding installed only in the low iota part (see figure 2). The radiation shield reduces the flux through the pumping gap because some of the neutrals are reflected towards the plasma. The consequence of the larger exhaust efficiency in the high-iota configuration is that twice more particles were exhausted via the AEP pumping line than via the AEH pumping line despite the lower effective pumping speed (11 800 vs 23 500 l s^{-1}).

We would like to compare the performance of the island divertor with the poloidal divertor of a tokamak. In ASDEX Upgrade, very high sub-divertor neutral pressures were obtained during H-mode operation. We quote from [21] (note that the pressure unit used here is Pa).

The neutral pressures required for the H-mode density limit studies are up to 6 Pa in the divertor and 0.06 Pa in the main chamber. This is more than twice than in a standard H-mode discharge (about 2 Pa in the divertor and 0.004 Pa in the main chamber). Note that the compression of the neutral gas in the divertor relative to the main chamber is lower by a factor of 5 for the H-mode density limit discharges.

These values can be directly compared to those obtained in this study. The poloidal divertor of ASDEX Upgrade enables a significantly higher neutral compression (100 … 500) than the island divertor of W7-X. The obtained maximum sub-divertor neutral pressure in ASDEX Upgrade is more than an order of magnitude higher than in the island divertor of W7-X (factor 30).

We try now to extrapolate the results to the next operation phase OP2.1. In OP2.1 the sub-divertor volumes will not be separated. Furthermore, pumping speed can be enhanced by the operation of the cryopumps with a maximum pumping speed 75 000 l s^{-1}. The total maximum pumping speed is 110 300 l s^{-1} (35 300 l s^{-1} from the turbo pumps and 75 000 l s^{-1} from the cryopumps).

Let us consider first the standard configuration. The maximum exhaust rate is given by $\Gamma_{ex} = 4 \times 10^{-4}$mbar $\times$ 109 000 l s^{-1} = 44 mbar l s^{-1} = 0.45×10^{21} molecules s^{-1}. In the high-iota configuration we will have a maximum exhaust rate of 1.5×10^{-3}mbar $\times$ 110 300 l s^{-1} = 165 mbar l s^{-1} = 1.8×10^{21} molecules s^{-1}. Note that the estimated exhaust rates are upper limits for two reasons. The first reason is that the pressure is not homogeneous in the sub-divertor volume. Therefore, the pressure might be lower at the various pumping locations compared to the maximum value used for the estimation. The second reason is that the divertor closure will be significantly lower by a factor of 4 in OP2.1.

We consider now an experiment with neutral beam injection in the standard configuration. Particle input of neutral beam heating is balanced by the estimated exhaust rate up to 5 MW. With a power of $P = 5$ MW and a mean energy

of $E = 50$ keV, an exhaust rate of $P/E = 0.6 \times 10^{21}$ particles s^{-1} must be maintained for steady state conditions, i.e. 0.3×10^{21} molecules s^{-1}. However, there will be additional particle sources such as pellet fueling and outgassing from the walls. A steady state operation will therefore depend on the detailed operation scenario and might be critical in the standard configuration. The high-iota configuration with its higher compression ratio and higher exhaust rates seems to be favorable from the viewpoint of particle exhaust.

7. Summary and conclusions

The development of robust pressure gauges with LaB_6 cathodes made reliable pressure measurements in the vessel of W7-X possible and allowed the characterization of the particle exhaust capability of the island divertor.

By the island divertor, a neutral particle compression of about 30 was achieved in the magnetic standard configuration, and about 80 in the high-iota configuration. The lower compression in the standard configuration was due to the low particle exhaust efficiency: only 0.44% of the particles hitting the divertor targets were pumped with a maximum exhaust flux of 9.4 mbar l^{-1}. In the high-iota configuration the exhaust efficiency was 2.9% and the maximum flux is 17.7 mbar 1 s^{-1}, i.e. twice as high despite the lower pumping speed via the AEP ports. The reason for the large differences is probably the low PCE in the magnetic standard configuration. Only 0.69% of the particles hitting the divertor targets entered the sub-divertor volume through the pumping gap. This allows two conclusions:

(a) In the high-iota configuration, the performance of the island divertor is good in terms of particle exhaust. However, the poloidal divertor of a tokamak is superior in this regard.

(b) An extrapolation to steady-state operation which is envisaged from operating phase two onwards shows that the high-iota configuration appears particularly promising whereas the standard configuration might be critical for operation with strong particle fueling as with NBI heating and pellet injection.

Acknowledgments

This work has been carried out within the framework of the EUROfusion Consortium, funded by the European Union via the Euratom Research and Training Programme (Grant Agreement No. 101052200—EUROfusion). Views and opinions expressed are however those of the author(s) only and do not necessarily reflect those of the European Union or the European Commission. Neither the European Union nor the European Commission can be held responsible for them.

We would like to thank the intern J. Maisano-Brown and the project team A. Graband, N. Rüter, and D. Pilopp for the valuable contributions.

Appendix. Uncertainty considerations

Some of the quantities used are subject to substantial uncertainty. We mention here in particular the particle fluxes to the walls, the effective pumping speeds, the pressure measurement itself, and the estimation of the particle removal efficiency PRE. We will provide uncertainty values for the measured or derived quantities and propagate them through the calculations.

We begin with the comparison of the exhausted flux in the two magnetic configurations. For this purpose we have to consider the uncertainty of the effective pumping speeds and the pressure measurement. The accuracy of the pressure measurement was estimated in [18]. It can be as large as $\pm 15\%$ due to jumps of the ion current in the strong magnetic field. The effective pumping speed was experimentally determined. The uncertainty is on the order of about $\pm 5\%$. The resulting uncertainty of the exhausted flux is $\pm 20\%$ for both configuration. However, as figures 5 and 6 show, there is a much larger scatter of the sub-divertor pressures in the magnetic standard configuration. The downward deviation occurs at lower heating powers. For the upward deviation we have no conclusive explanation so that we have to assume an additional uncertainty interval of $+50\%$ for the standard configuration and $+20\%$ for the high-iota configuration. This gives for the exhausted fluxes in the magnetic standard configuration 9.4 mbar 1 s^{-1} $(-20 \ldots +70\%)$ and for the high-iota configuration 18 mbar 1 s^{-1} $(-20 \ldots 40\%)$. Consequently, the difference of the exhausted fluxes in both configurations are statistically significant. This applies all the more to the exhaust efficiencies in both configurations.

We continue with the estimation of the uncertainty of the exhaust efficiencies. The deviation of the *S*/*XB* value for the wall fluxes of hydrogen was studied in detail in [3]. It is about $\pm 10\%$ which is also the uncertainty of the target fluxes. The uncertainty of the exhausted flux was estimated above to $\pm 20\%$. This results in an uncertainty of 30% for the exhaust efficiencies.

Note that we already estimated the uncertainty of the PCE in the standard configuration to be 15%. Furthermore, there we mentioned a systematic error which could be as large as -20%.

Finally we derive the uncertainty intervals of the neutral compression. The accuracy of the pressure measurement itself results in an uncertainty interval of $\pm 30\%$. When we add the uncertainty from the scatter plots we arrive at the following intervals: $-30 \ldots +80\%$ for the standard configuration and $-30 \ldots +50\%$ for the high-iota configuration. Figure 13 shows that these intervals have almost no overlap, i.e. the difference of the compression in both configurations is statistically relevant.

ORCID iDs

U. Wenzel https://orcid.org/0000-0002-4107-9291
G. Schlisio https://orcid.org/0000-0002-5430-0645
P. Drewelow https://orcid.org/0000-0003-0121-9058
T.S. Pedersen https://orcid.org/0000-0002-9720-1276

S. Bozhenkov https://orcid.org/0000-0003-4289-3532
A.K. Kharwandikar https://orcid.org/0000-0001-7272-1198
S. Lazerson https://orcid.org/0000-0001-8002-0121
D. Naujoks https://orcid.org/0000-0003-4265-6078
V. Perseo https://orcid.org/0000-0001-8473-9002
V. Winters https://orcid.org/0000-0001-8108-7774

References

[1] Pedersen T.S. *et al* 2016 Confirmation of the topology of the Wendelstein 7-X magnetic field to better than 1:100 000 *Nat. Commun.* **7** 13493

[2] Pedersen T.S. *et al* 2019 First results from divertor operation in Wendelstein 7-X *Plasma Phys. Control. Fusion* **61** 014035

[3] Kremeyer T. *et al* 2022 Analysis of hydrogen fueling, recycling, and confinement at Wendelstein 7-X via a single-reservoir particle balance *Nucl. Fusion* **62** 036023

[4] Schlisio G. *et al* 2021 The evolution of the bound particle reservoir in Wendelstein 7-X and its influence on plasma control *Nucl. Fusion* **61** 036031

[5] Renner H., Sharma D., Kißlinger J., Boscary J., Grote H. and Schneider R. 2004 Physical aspects and design of the Wendelstein 7-X divertor *Fusion Sci. Technol.* **46** 2

[6] Andreeva T., Kisslinger J. and Wobig H. 2002 Characteristics of main configurations of Wendelstein 7-X *Probl. At. Sci. Technol., Ser.: Plasma Phys.* **4** 45–7

[7] Grote H., Kisslinger J., Renner H., Boscary J., Greuner H., Hoffmann F.W. and Mendelevitch B. 2003 Neutral particle modelling and particle exhaust in the Wendelstein 7-X stellarator *J. Nucl. Mater.* **313–316** 1298

[8] Sharma D. *et al* 2003 Optimization of the W7-X pumping system *30th EPS Conf. Controlled Fusion and Plasma Physics* (St. Petersburg , 7–11 July 2003) **vol 27 A** ECA P-1.14 (https://pure.mpg.de/rest/items/item_2137671_3/component/file_3311242/content)

[9] Barbui T., Bozhenkov S., Effenberg F., Favreau F., Flom E. and Fuchert G. 2019 The He/Ne beam diagnostic for line-ratio spectroscopy in the island divertor of Wendelstein 7-X *J. Instrum.* **14** C07014

[10] Behringer K., Summers H.P., Denne B., Forrest M. and Stamp M. 1989 Spectroscopic determination of impurity influx from localized surfaces *Plasma Phys. Control. Fusion* **31** 2059–99

[11] Brezinsek S., Sergienko G., Pospieszczyk A., Mertens P., Samm U. and Greenland P.T. 2005 Characterization of the deuterium recycling flux in front of a graphite surface in the TEXTOR tokamak *Plasma Phys. Control. Fusion* **47** 615–34

[12] Haas G. and Bosch H.-S. 1998 In vessel pressure measurement in nuclear fusion experiments with ASDEX gauges *Vacuum* **51** 39–46

[13] Johnson L.C. and Hinnov E. 1973 Ionization, recombination, and population of excited levels in hydrogen plasmas *J. Quant. Spectrosc. Radiat. Transfer* **13** 333–58

[14] Jakubowski M. *et al* 2021 Overview of the results from divertor experiments with attached and detached plasmas at Wendelstein 7-X and their implications for steady-state operation *Nucl. Fusion* **61** 106003

[15] Schmitz O. *et al* 2021 Stable heat and particle flux detachment with efficient particle exhaust in the island divertor of Wendelstein 7-X *Nucl. Fusion* **61** 016026

[16] Lazerson S.A. *et al* 2019 Tuning of the rotational transform in Wendelstein 7-X *Nucl. Fusion* **59** 126004

[17] Wenzel U., Pedersen T.S., Marquardt M. and Singer M. 2018 An ionization pressure gauge with LaB_6 emitter for long-term operation in strong magnetic fields *Rev. Sci. Instrum.* **89** 033503

[18] Wenzel U., Schlisio G., Mulsow M., Pedersen T.S., Singer M., Marquardt M., Pilopp D. and Rüter N. 2019 Performance of new crystal cathode pressure gauges for long-pulse operation in the Wendelstein 7-X stellarator *Rev. Sci. Instrum.* **90** 123507

[19] Wenzel U., Schlisio G., Pedersen T.S., Marquardt M., Pilopp D., Rüter N. and Graband A. 2021 On the stability of thoriated tungsten cathodes in strong magnetic fields *Rev. Sci. Instrum.* **92** 083510

[20] Winters V.R. *et al* 2021 EMC3-EIRENE simulation of first wall recycling fluxes in W7-X with relation to H-alpha measurements *Plasma Phys. Control. Fusion* **63** 045016

[21] Bernert M. 2013 Analysis of the H-mode density limit in the ASDEX Upgrade tokamak using bolometry *PhD Thesis* LMU München (https://edoc.ub.uni-muenchen.de/16262/1/BernertRSMatthias.pdf)